Journal Club 2011/05/16 Toshiya Namikawa

A **Weak lensing reconstruction through cosmic magnification I: a minimal variance map reconstruction**

X. Yang & Z. Pengjie arXiv:1105.2385

B **The Primordial Inflation Explorer (PIXIE): A Nulling Polarimeter for Cosmic Microwave Background Observations**

A. Kogut *et al* arXiv:1105.2385

C1 **The Atacama Cosmology Telescope: Detection of the Power Spectrum of Gravitational Lensing**

S. Das *et al* arXiv:1103.2124

C2 **The Atacama Cosmology Telescope: Evidence for Dark Energy from the CMB Alone**

B. Sherwin *et al* arXiv:1105.0419

A

$$\delta C_{\rm bb}^{(3)} = C_{\rm m_b m_b} \times \left[\sum_j \left\langle (\delta b_j^{\rm b})^2 \right\rangle \left(\sum_i \frac{\partial w_i^{\rm b}}{\partial b_j^{\rm b}} b_i^{\rm b} \right)^2 + \left(\sum_i w_i^{\rm b} b_i^{\rm b} \right) \left(\sum_j \langle (\delta b_j^{\rm b})^2 \rangle \sum_i \frac{\partial^2 w_i^{\rm b}}{\partial b_j^{\rm b} \partial b_j^{\rm b}} b_i^{\rm b} \right) - \sum_k \langle (\delta b_k^{\rm b})^2 \rangle \sum_{ij} \frac{\partial w_i^{\rm b}}{\partial b_k^{\rm b}} \frac{\partial w_j^{\rm b}}{\partial b_k^{\rm b}} b_i^{\rm b} b_j^{\rm b} \Delta r_{ij} \right] + C_{\rm m_b \kappa_b} \times \left[\sum_j \langle (\delta b_j^{\rm b})^2 \rangle \sum_i \frac{\partial^2 w_i^{\rm b}}{\partial b_z^{\rm b} \partial b_z^{\rm b}} b_i^{\rm b} \right] . \quad (30)$$

$$\delta C_{\rm bf}^{(3)} = \frac{1}{2} C_{\rm m_f \kappa_b} \times \left[\sum_j \langle (\delta b_j^{\rm f})^2 \rangle \sum_i \frac{\partial^2 w_i^{\rm f}}{\partial b_j^{\rm f} \partial b_j^{\rm f}} b_i^{\rm f} \right] . \quad (31)$$

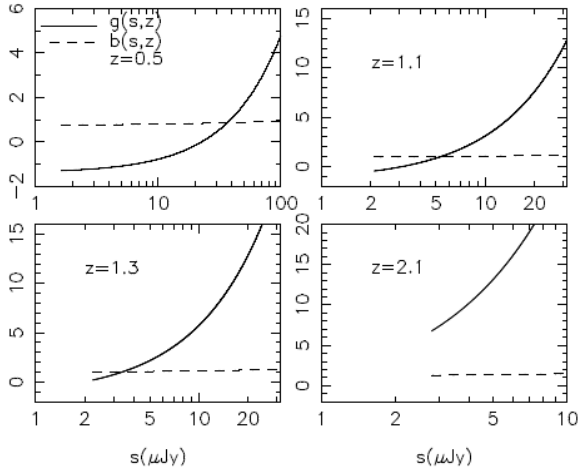

Figure 3. The HI galaxy bias $b(s,z)$ and the magnification bias $g(s,z) = 2(\alpha - 1)$ as a function of flux s by fixing the redshift to be the central value of each redshift bin. The plotted curves are started from the flux limit at the fixed redshift. The cosmic magnification bias strongly depends on the flux, while the galaxy bias weakly changes with it. Such difference in flux dependence ensures us to find a optimal estimator to reconstruct the weak lensing from the cosmic magnification.

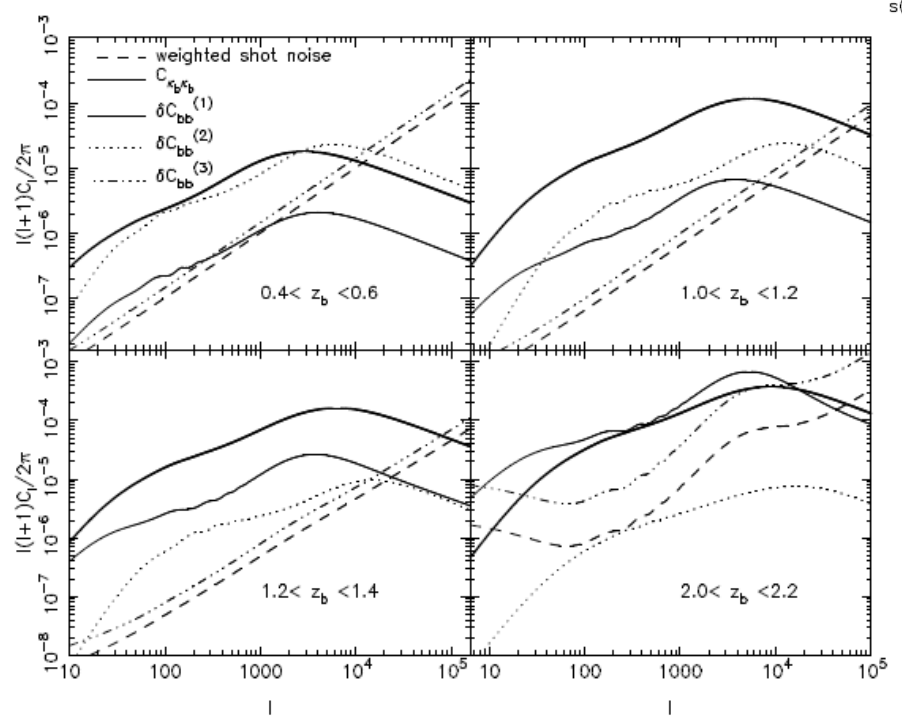

Figure 6. Composition of the reconstructed weak lensing power spectrum for the same redshift bin. We plot the weak lensing power spectrum $C_{\kappa_b\kappa_b}$ by bold solid line. The three types of systematical errors $\delta C_{\rm bb}^{(1)}$ from error in deterministic galaxy bias, $\delta C_{\rm bb}^{(2)}$ from the stochastic bias, and $\delta C_{\rm bb}^{(3)}$ from the shot noise are presented by the solid, dotted and dash-dot-dot-dotted lines, respectively. While statistical error is plotted by the dashed line. Here the statistical error is called weighted shot noise only from the sparse galaxy distribution, since we aim to reconstruct the weak lensing at each angular pixel with the corresponding cosmic variance. For the intermediate redshift bins $1.0 < z_{\rm b} < 1.2$ and $1.2 < z_{\rm b} < 1.4$, the signal overwhelms all these errors which can be controlled to $\sim 10\%$-20% level.

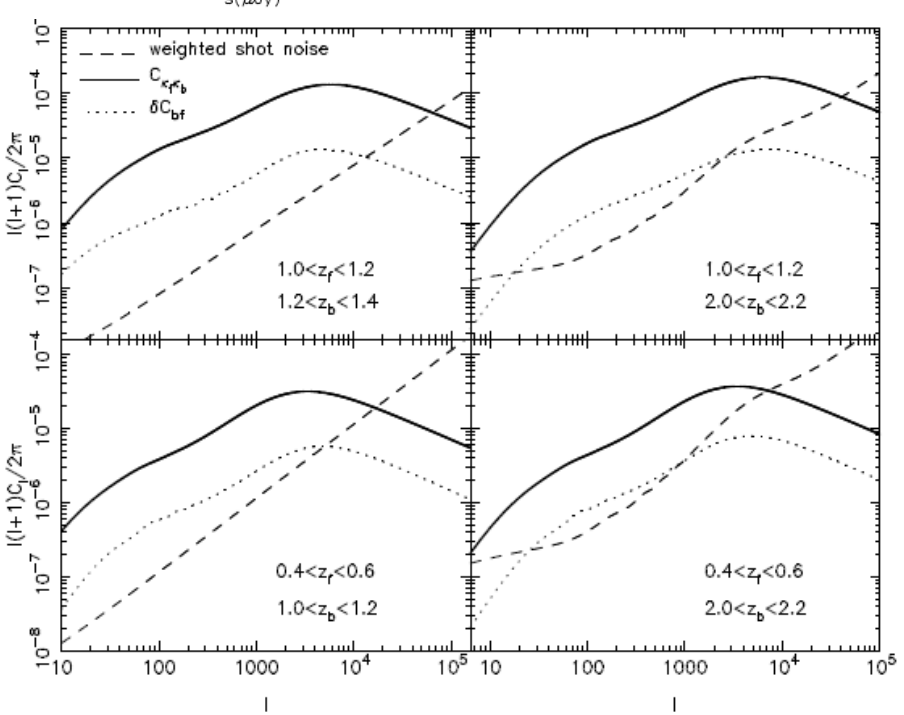

Figure 7. The weak lensing signal, the systematical error and the statistical error in the weak lensing reconstruction from the foreground and background redshift bins. The solid line is the cross-correlation power spectrum of cosmic convergence. The dotted line represents the systematical error combing three types $\delta C_{\rm bf} = \delta C_{\rm bf}^{(1)} + \delta C_{\rm bf}^{(2)} + \delta C_{\rm bf}^{(3)}$ and the dashed line corresponds to the weighted shot noise. In $\delta C_{\rm bf}$, $\delta C_{\rm bf}^{(1)}$ from the deterministic galaxy bias is dominant and the systematical error from the stochastic bias can be avoided in such cross lensing power spectrum, namely $\delta C_{\rm bf}^{(2)} = 0$. For every couple of foreground and background redshift bins, the cross reconstructed weak lensing signal dominates at scale range $10 \lesssim \ell \lesssim 10^4$ and it can be measured to reach $\sim 10\%$-20% accuracy.

B

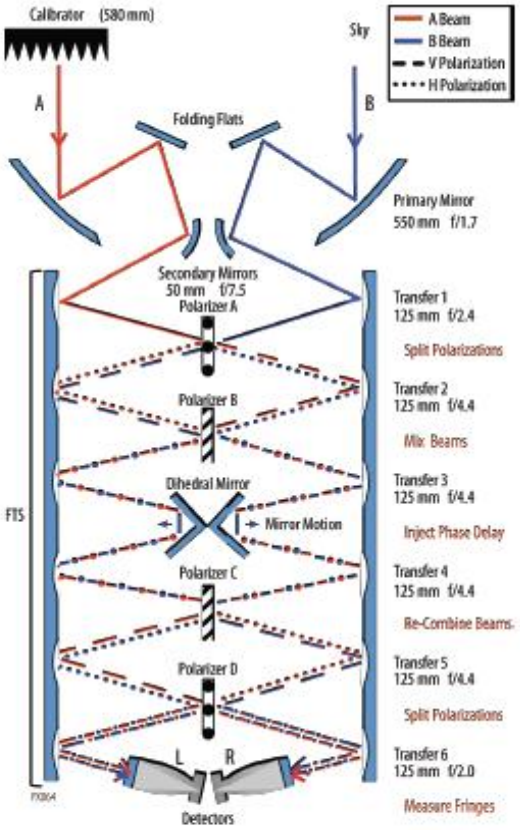

Figure 2. PIXIE optical signal path. As the dihedral mirrors move, the detectors measure a fringe pattern proportional to the Fourier transform of the difference spectrum between orthogonal polarization states from the two input beams (Stokes Q in instrument coordinates). A full-aperture blackbody calibrator can move to block either input beam, or be stowed to allow both beams to view the same patch of sky.

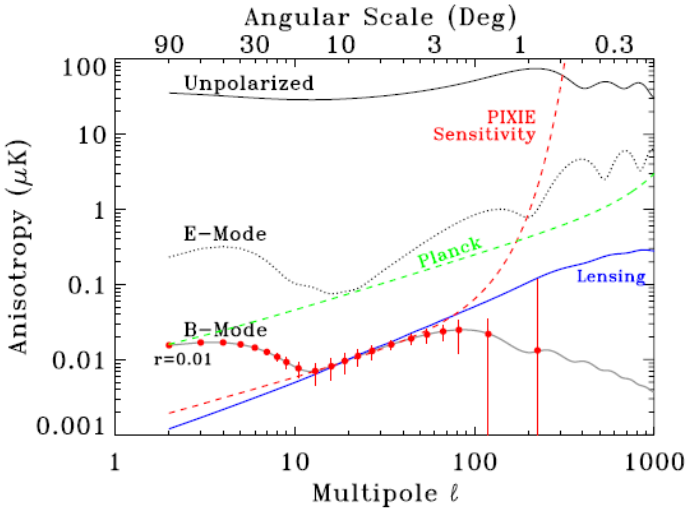

Figure 1. Angular power spectra for unpolarized, E-mode, and B-mode polarization in the cosmic microwave background. The dashed red line shows the PIXIE sensitivity to B-mode polarization at each multipole moment $\ell \sim 180°/\theta$. The sensitivity estimate assumes a 4-year mission and includes the effects of foreground subtraction within the cleanest 75% of the sky combining PIXIE data at frequencies $\nu < 600$ GHz. Red points and error bars show the response within broader ℓ bins to a B-mode power spectrum with amplitude $r = 0.01$. PIXIE will reach the confusion noise (blue curve) from the gravitational lensing of the E-mode signal by cosmic shear along each line of sight, and has the sensitivity and angular response to measure even the minimum predicted B-mode power spectrum at high statistical confidence.

Table 2. Observatory CMB Sensitivity

Observing Mode	NET (μK $s^{1/2}$)	NEQ (μK $s^{1/2}$)
Calibrator Deployed	13.6	19.2
Calibrator Stowed	—	5.6

C1

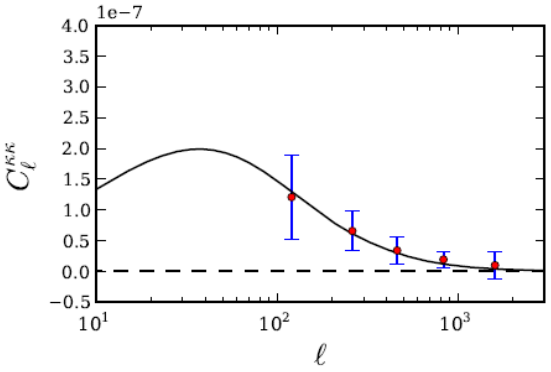

FIG. 1. Mean convergence power spectrum (red points) from 480 simulated lensed maps with noise similar to our data. The solid line is the input lensing power spectrum, taken from the best-fit WMAP+ACT cosmological model. Error bars correspond to the scatter of power spectrum values obtained from individual maps.

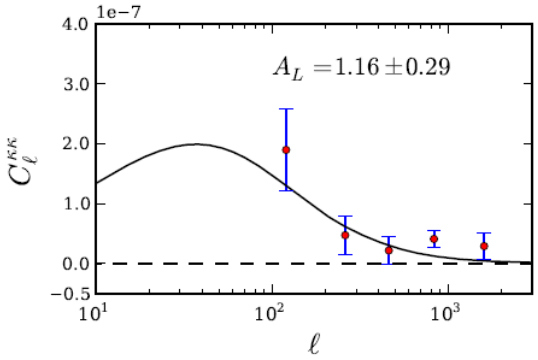

FIG. 2. Convergence power spectrum (red points) measured from ACT equatorial sky patches. The solid line is the power spectrum from the best-fit WMAP+ACT cosmological model with amplitude $A_L = 1$, which is consistent with the measured points. The error bars are from the Monte Carlo simulation results displayed in Fig. 1. The best-fit lensing power spectrum amplitude to our data is $A_L = 1.16 \pm 0.29$

C2

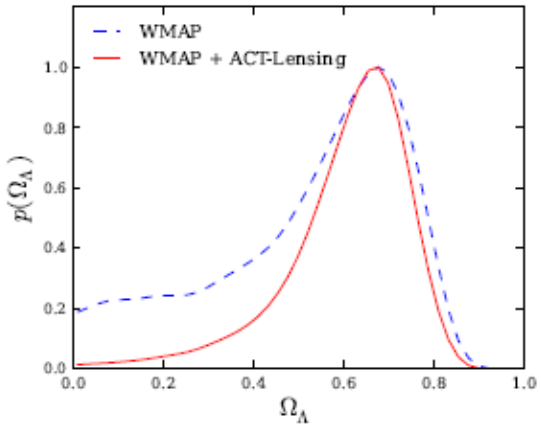

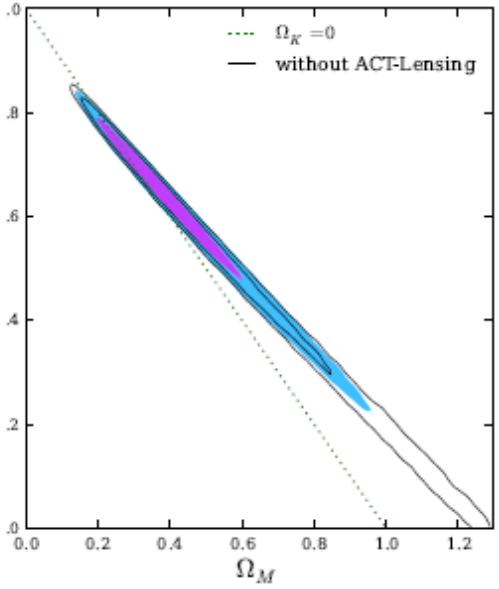

FIG. 3. Upper panel: Two-dimensional marginalized posterior probability for Ω_m and Ω_Λ (68% and 95% C.L.s shown). Colored contours are for WMAP + ACT Lensing, black lines are for WMAP only. Using WMAP data alone, universes with $\Omega_\Lambda = 0$ lie within the 95% C.L. The addition of lensing data breaks the degeneracy, favoring models with dark energy. Lower panel: One-dimensional marginalized posterior probability for Ω_Λ (not normalized). An energy density of $\Omega_\Lambda \simeq 0.7$ is preferred even from WMAP alone, but when lensing data are included, an $\Omega_\Lambda = 0$ universe is strongly disfavoured.

Wakate Cosmo Semi 2011/05/17

Toshiya Namikawa

1 **Reconstruction of Cosmic Magnification from Galaxy Number Counts**

X. Yang & Z. Pengjie arXiv:1105.2385

2 **Measurement of CMB Lensing from ACT Temperature Map and Cosmological Implications**

S. Das *et al* arXiv:1103.2124

B. Sherwin *et al* arXiv:1105.0419

1. イントロ

☆ Cosmic Magnification

銀河の測光サーベイにおいて、観測される銀河の個数密度
が重力レンズで変更を受ける効果

$$\delta_g^{obs}(z,\hat{\theta}) = b\delta_m(z,\hat{\theta}) + g(z)\kappa(z,\hat{\theta}) \qquad \left(\delta_g^{obs}(z,\hat{\theta}) \equiv \frac{n_g(z,\hat{\theta}) - \bar{n}_g(z)}{\bar{n}_g(z)}\right)$$

銀河バイアス

物質密度揺らぎ

Convergence

増光係数（？）

$$g(z) \equiv -2\frac{d\ln \bar{n}_g(z,<m)}{d\,m} - 4$$

(e.g. Matsubara'00)

<u>κを取り出すことで、重力レンズ効果を通じた宇宙論の情報が得られる</u>

☆ Cosmic Shear との比較

・**銀河の形状を測る必要がない**

銀河固有の歪み、PSF補正などの系統誤差を含まない

・**Cosmic Shear とは独立な情報**

2. 測定方法の提案

☆ Estimator

複数のmagnitude-binでδ_g^{obs}を測定し、それらを組み合わせてκを推定する

magnitude-bin (i)で和をとる

$$\hat{\kappa}(z,\hat{\theta}) \equiv \sum_i w_i(z)\delta_{g,i}^{obs}(z,\hat{\theta})$$

Weight Function

（＊）Weight Function は以下の条件で決められた関数

1. バイアスしない　　$\langle\hat{\kappa}\rangle = \kappa$

2. Estimator で見積もったκの分散を最小にする　　（つまり $\langle(\hat{\kappa}-\kappa)^2\rangle$ が最小）

この結果、

$$w_i = \frac{\bar{n}_{g,i}}{2}(A_i g_i + B_i b_i)$$

$$A_i = \frac{-2\sum_i \bar{n}_{g,i} b_i^2}{\left(\sum_i \bar{n}_{g,i} b_i g_i\right)^2 - \sum_i \bar{n}_{g,i} b_i^2 \sum_i \bar{n}_{g,i} g_i^2}$$

$$B_i = \frac{2\sum_i \bar{n}_{g,i} b_i g_i}{\left(\sum_i \bar{n}_{g,i} b_i g_i\right)^2 - \sum_i \bar{n}_{g,i} b_i^2 \sum_i \bar{n}_{g,i} g_i^2}$$

（b_i の推定は次のスライド）

☆ 銀河バイアスの推定

帰納的に推定する

Step 1. 重力レンズの寄与は無視できる（$\delta_{g,i}^{obs} \simeq b_i \delta_m$）と考え、

$$b_i^2 \langle |\delta_m|^2 \rangle = \langle \left|\delta_{g,i}^{obs}\right|^2 \rangle$$

からb_iを求め（これを$b_i^{(1)}$とする）、これから weight function $w_i^{(1)}$ 、convergence $\kappa^{(1)}$ を計算

✓ 論文ではコメントされていないが、左辺のパワースペクトル $\langle |\delta_m|^2 \rangle$ は、重力レンズを受けていないと仮定して推定した宇宙論パラメータから計算すれば良い（？）

Step 2. 重力レンズの寄与を$\delta_{g,i}^{obs} \simeq b_i \delta_m + g_i \kappa^{(1)}$として取り入れ、

$$b_i^2 \langle |\delta_m|^2 \rangle = \langle \left|\delta_{g,i}^{obs} - g_i \kappa^{(1)}\right|^2 \rangle$$

からb_iを求め（これを$b_i^{(2)}$とする）、これから weight function $w_i^{(2)}$ 、convergence $\kappa^{(2)}$ を計算

✓ 左辺のパワースペクトル $\langle |\delta_m|^2 \rangle$ は、$\delta_{g,i}^{obs} \simeq b_i \delta_m + g_i \kappa^{(1)}$と仮定して推定した宇宙論パラメータから計算すれば良い（？）

Step 3. 繰り返す（最終的に$b_i^{(n)}, \kappa_i^{(n)}$ が得られる）

3. 再構築における誤差

redshift-bin α と β の銀河の相関を考える

◆ 統計誤差

Shot noise のみを考えると

$$\Delta C_\ell^{\alpha\beta} = \sqrt{\frac{1}{(2\ell+1)f_{sky}}} \sqrt{\sum_i \frac{\left(w_i^\alpha\right)^2}{\bar{n}_i^\alpha} \sum_i \frac{\left(w_i^\beta\right)^2}{\bar{n}_i^\beta}}$$

◆ 系統誤差

1 $\langle b_i^{(n)} - b_i^{true} \rangle \neq 0$ によって引き起こされる誤差 $\delta C^{(1)}$

2 Stochastic bias（ b_i の相関係数が$r_{ij} \neq \delta_{ij}$ ）によって引き起こされる誤差 $\delta C^{(2)}$

3 $\langle b_i^{(n)} - b_i^{true} \rangle = 0$ でも$\langle \left| b_i^{(n)} - b_i^{true} \right|^2 \rangle \neq 0$ によって引き起こされる誤差 $\delta C^{(3)}$

4. シグナルに対する誤差の影響

- 想定するサーベイ・デザイン

  SKA-like なサーベイを想定

  - $f_{sky} = 0.25\ (10000\ \mathrm{deg}^2)$
  - $z = 0$~2の範囲の銀河を約10^8個測定。

g, b のモデル

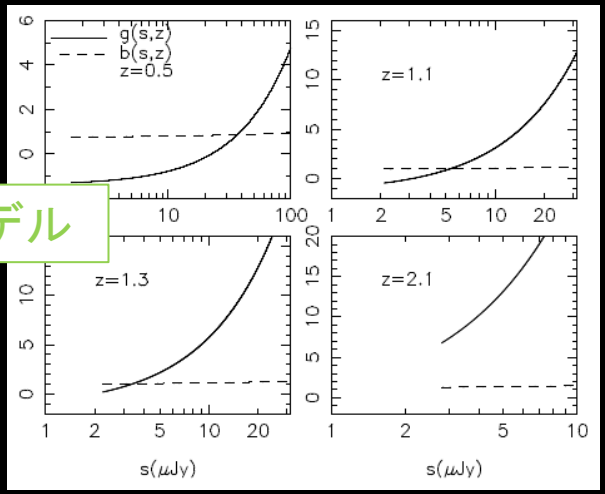

Auto-Correlation

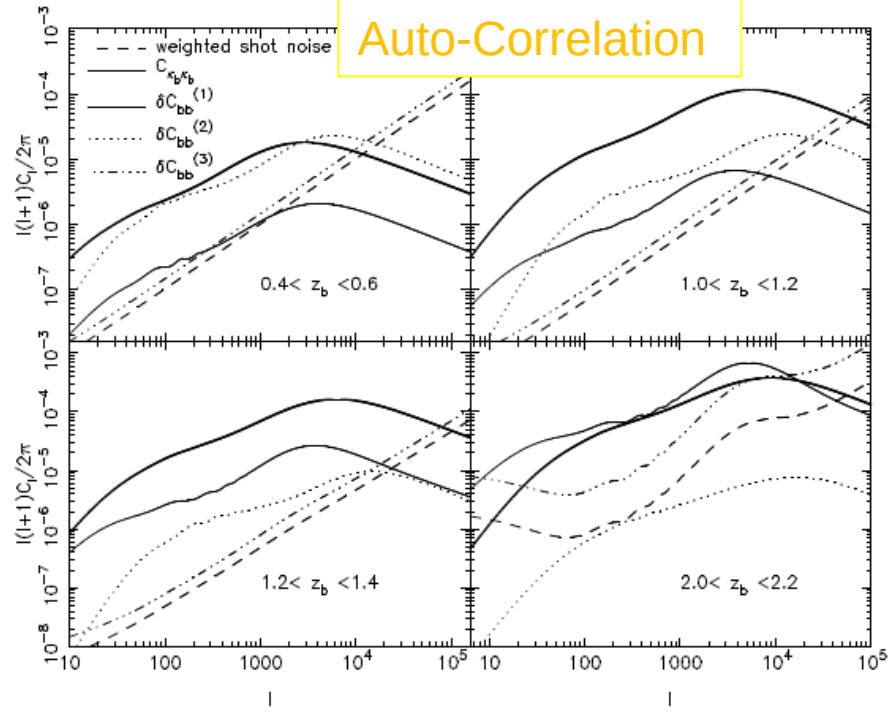

Cross-Correlation

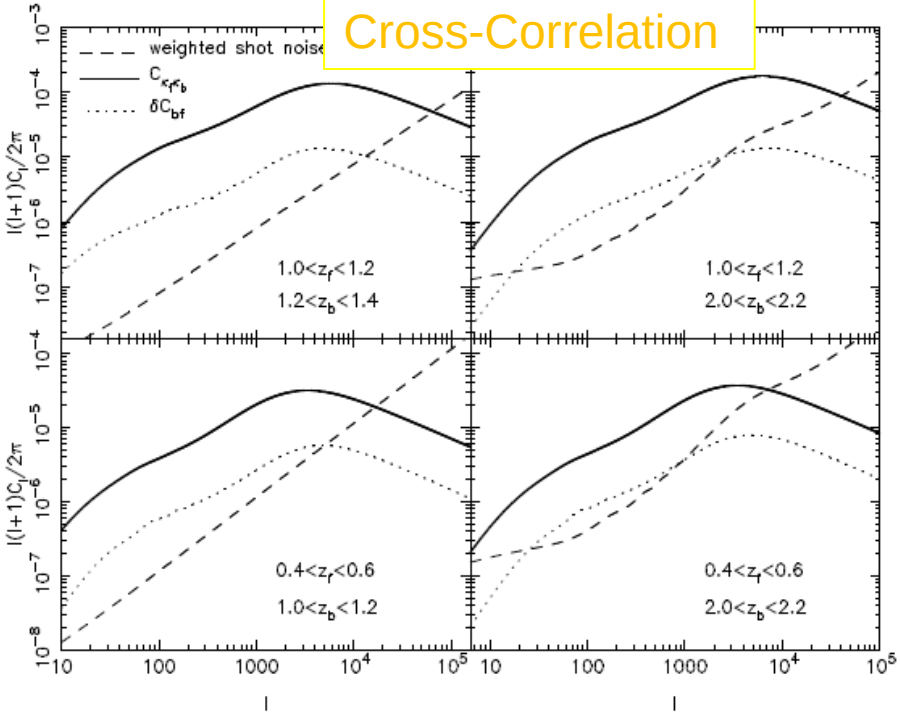

- High-z ほどシグナルに比べて誤差が大きくなる
- Cross-Correlation のほうが誤差が小さく抑えられる